

# Unveiling Nanometer Scale Extinction and Scattering Phenomena through Combined Electron Energy Loss Spectroscopy and Cathodoluminescence Measurements

Arthur Losquin,<sup>†,‡</sup> Luiz F. Zagonel,<sup>†,§</sup> Viktor Myroshnychenko,<sup>||,⊥</sup> Benito Rodríguez-González,<sup>¶</sup> Marcel Tencé,<sup>†</sup> Leonardo Scarabelli,<sup>#</sup> Jens Förstner,<sup>⊥</sup> Luis M. Liz-Marzán,<sup>#,¶,○</sup> F. Javier García de Abajo,<sup>▽,◆</sup> Odile Stéphan,<sup>†</sup> and Mathieu Kociak\*,<sup>†</sup>

<sup>†</sup>Laboratoire de Physique des Solides CNRS/UMR8502, Bâtiment 510, University Paris-Sud, Orsay 91405, France

<sup>‡</sup>Department of Physics, Lund University, P.O. Box 118, SE-221 00 Lund, Sweden

<sup>§</sup>Instituto de Física Gleb Wataghin, Universidade Estadual de Campinas, Unicamp, Campinas, São Paulo 13083-970, Brazil

<sup>||</sup>Instituto de Química-Física - CSIC, Serrano 119, 28006 Madrid, Spain

<sup>⊥</sup>Institute of Electrical Engineering, University of Paderborn, Warburger Strasse 100, D-33098 Paderborn, Germany

<sup>¶</sup>Departamento de Química Física, Universidad de Vigo, 36310 Vigo, Spain

<sup>#</sup>Bionanoplasmonics Laboratory, CIC biomaGUNE, Paseo de Miramón 182, 20009 Donostia-San Sebastián, Spain

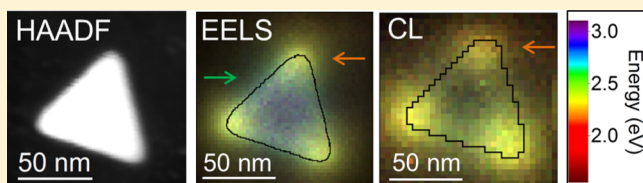
<sup>▽</sup>ICFO-Institut de Ciències Fotoniques, Mediterranean Technology Park, 08860 Castelldefels (Barcelona), Spain

<sup>○</sup>Ikerbasque, Basque Foundation for Science, 48013 Bilbao, Spain

<sup>◆</sup>ICREA-Institució Catalana de Recerca i Estudis Avançats, Passeig Lluís Companys, 23, 08010 Barcelona, Spain

## Supporting Information

**ABSTRACT:** Plasmon modes of the exact same individual gold nanoprisms are investigated through combined nanometer-resolved electron energy-loss spectroscopy (EELS) and cathodoluminescence (CL) measurements. We show that CL only probes the radiative modes, in contrast to EELS, which additionally reveals dark modes. The combination of both techniques on the same particles thus provides complementary information and also demonstrates that although the radiative modes give rise to very similar spatial distributions when probed by EELS or CL, their resonant energies appear to be different. We trace this phenomenon back to plasmon dissipation, which affects in different ways the plasmon signatures probed by these techniques. Our experiments are in agreement with electromagnetic numerical simulations and can be further interpreted within the framework of a quasistatic analytical model. We therefore demonstrate that CL and EELS are closely related to optical scattering and extinction, respectively, with the addition of nanometer spatial resolution.



**KEYWORDS:** *nanooptics, plasmonics, electron energy loss spectroscopy, cathodoluminescence, bright and dark modes, light scattering*

The last two decades have witnessed impressive advances in the synthesis of a vast range of nanoobjects with new and intriguing optical properties that are strongly dependent on their exact shape, size, composition, and local environment, opening new possibilities within the active field of nanooptics. Understandably, advances in this field have been largely fuelled by the availability of techniques that address optical properties at the nanometer scale, as well as new theoretical and simulation tools. Previously unexplored fundamental issues are raised, and in particular the classical optical concepts of extinction, absorption, and scattering are no longer sufficient to describe optical phenomena at the nanoscale. Instead, the spatial and spectral distributions of photonic eigenmodes have been recognized to play an important role when interpreting experimental outputs delivered by numerous near-field techniques.<sup>1–8</sup> Likewise, concepts such as the local density of

optical states (LDOS)<sup>9</sup> or alternative descriptions in terms of modal decompositions<sup>10</sup> have become relevant for understanding nanoscale-resolved experiments, including scanning near-field optical microscopy,<sup>11,12</sup> thermal radiation scanning tunnelling microscopy,<sup>13</sup> electron energy-loss spectroscopy (EELS),<sup>12,14–20</sup> and cathodoluminescence (CL).<sup>16,17,21,22</sup> Nevertheless, the physics embodied in optical extinction, absorption, and scattering phenomena should hold, to some extent, at the nanometer scale. In other words, we still need to understand how a nanostructure absorbs and scatters electromagnetic waves at subwavelength scales. An experimental and

**Received:** November 14, 2014

**Revised:** January 4, 2015

**Published:** January 20, 2015

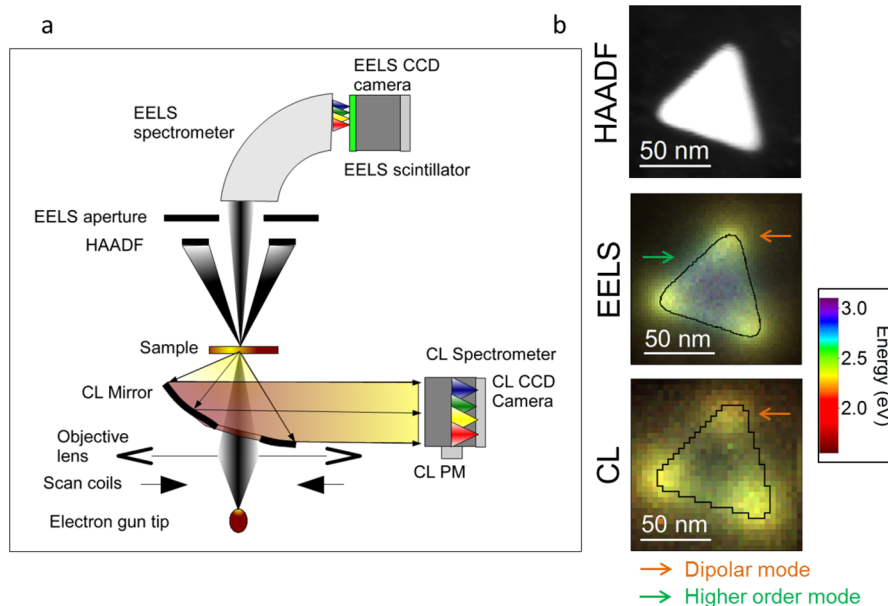


**Figure 1.** (a) Scheme of a scanning transmission electron microscope equipped with EELS and CL detection systems. (b) Combined HAADF imaging (top), EELS (middle), and CL (bottom) spatially resolved data sets. Total acquisition times are 157 s for CL and 16 s for EELS. In the case of EELS, the spectra are first deconvolved and normalized. The CL and EELS images are generated by coloring each filtered maps of the data sets according to its energy, weighing each pixel of the maps by its intensity and summing all the resulting images. This simplified representation of the EELS and CL data sets straightforwardly shows that the EELS data exhibit both dipolar and higher order modes, whereas the CL data exhibit mainly the dipolar mode. The black lines superimposed on the maps indicate the prism shape as obtained from the HAADF image.

theoretical framework reconciling both approaches, thus, is necessary.

EELS and CL, which have proved to be outstanding tools for studying surface plasmons (SP) with superior spatial resolution even in the most complex systems,<sup>23</sup> are suitable candidates to address these issues.<sup>24</sup> In these techniques, a fast electron (typically traveling at half the speed of light) is focused onto or close to the nanostructure of interest. The electron is capable of transferring energy to the nanostructure via electromagnetic interaction.<sup>25</sup> This amount of energy is measured by analyzing the stopping experienced by the electron in EELS or by detecting the emitted light resulting from the interaction in CL. Therefore, it is basically the electromagnetic nature of the electron-sample interaction that allows us to explore the optical response of the nanostructure. In particular, CL relates to the ability of the nanostructure to scatter the evanescent electromagnetic field carried by the electron into the far field, whereas EELS probes the sum of radiative losses (i.e., CL) plus energy transfers that are inelastically absorbed by the materials involved. This close relationship between fast-electron-based spectroscopies and optical properties has been emphasized in qualitative interpretations of EELS and CL experiments in terms of either absorption, extinction, or scattering.<sup>26–30</sup> However, the apparent connection between EELS and extinction on the one hand and CL and scattering on the other hand, which is also suggested by modal decomposition analyses in the case of spheres,<sup>16,24</sup> has not been addressed theoretically in a general case. From the experimental viewpoint, we remark that combined EELS/CL experiments on the same nanoobject and in the same environment are still missing, precluding a fair, exact comparison of both techniques. Thus, we still lack a direct proof of the possibility of measuring optical extinction and scattering at the nanometer scale, as well as a clear evidence of the intimate relationship between

traditional optics-based measurements and subwavelength-resolved electron-beam spectroscopies.

In this article, we present experimental and theoretical evidence that spatially resolved EELS and CL experiments performed on the same individual metallic nanoparticles allow us to directly disentangle radiative and nonradiative modes on an individual particle basis. We also show that EELS and CL are closely connected to optical extinction and scattering phenomena at the nanometer scale. By collecting nanometer-resolved EELS and CL spectra from the same individual small gold triangular nanoparticles, we first demonstrate that only the dipolar mode is measured by both techniques, whereas the higher order modes are only accessible through EELS. This is a clear experimental signature of the inability of CL to detect nonradiative modes, in contrast to EELS. We further demonstrate that dipolar SP modes, as measured by both techniques, may appear to have different resonance energies although they give rise to similar intensity spatial distributions. Simulations clearly show that such spectral differences between EELS and CL are also present in light extinction and scattering. As a consequence, the main spectral differences between extinction and scattering observed when examining individual nanoparticles *as a whole* via far-field spectroscopies are qualitatively maintained upon nanoscale inspection *within* individual nanoparticles through EELS and CL. We formulate modal decompositions in the quasistatic limit for CL, as well as for optical extinction and scattering, and compare them to a previously derived formula for EELS. This helps us to understand in simple terms the role of dissipation that we report in both experiments and simulations, which affects extinction and scattering phenomena in distinct ways.

Gold triangular nanoprisms are synthesized using a seed-mediated growth in aqueous media;<sup>31,32</sup> briefly, a small amount of iodide ions is exploited to guide the two-step growth of gold seeds stabilized by cetyltrimethylammonium chloride toward

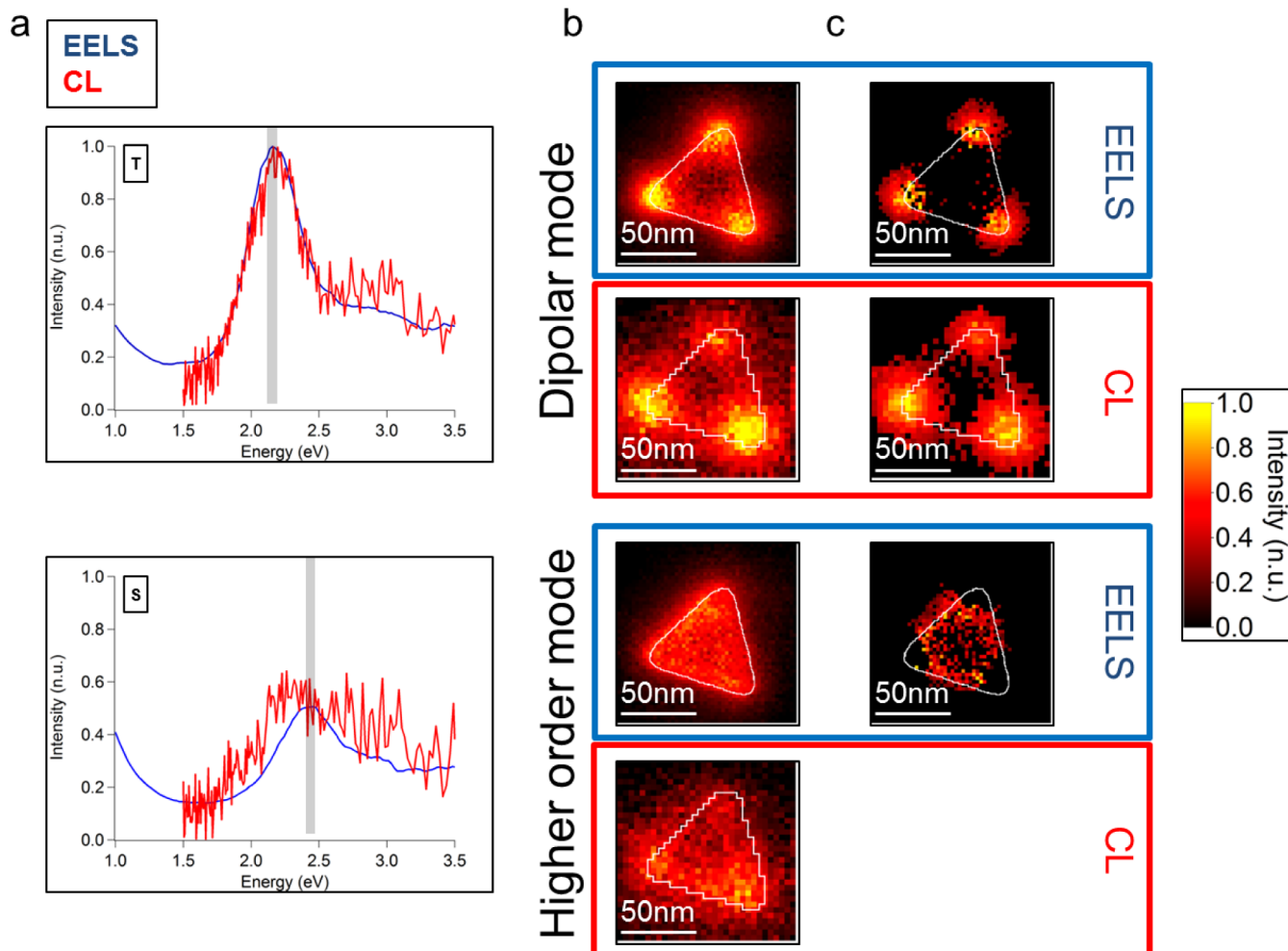


**Figure 2.** (a) EELS (blue) and CL (red) spectra taken at the low left tip (T) and left side (S) of the 60 nm long, 30 nm thick prism deposited on a graphene sheet shown on Figure 1. The vertical gray windows indicate the spectral ranges considered when building the energy filtered and fitted maps. The spectra are averaged on 9 (EELS) and 25 (CL) pixels of the data sets. (b) EELS and CL maps filtered around the energy of the EELS/CL maxima shown on the T and S panels of (a). (c) Fitted amplitude maps corresponding to the dipolar (EELS and CL) and higher order (EELS only) modes. EELS and CL are independently normalized to their own maxima. The white lines superimposed on the maps indicate the prism shape as obtained from the HAADF image.

the final triangular shape. In this study, two batches of nanoprisms are used. The first one<sup>32</sup> consists of monodisperse equilateral 60 nm edge long, 30 nm thick nanoprisms deposited on a graphene sheet. The second one<sup>31</sup> consists of 80–200 nm edge long (and varying thickness) nanoprisms drop-casted on a thin carbon film. Such nanoparticles are chosen for their high crystallinity, which leads to well-defined resonances both in EELS<sup>33</sup> and CL<sup>34</sup> and because the SP modes that dominate their optical response have been thoroughly discussed in the literature.<sup>20,27,33,35</sup> In particular, in small nanoprisms (such as the 60 nm long ones), the modes are rather simple<sup>35</sup> and well described in the quasistatic limit.<sup>20,27</sup> Additionally, the mode energies lie within the experimental range that is accessible with our CL detection system (above 1.2 eV). However, these nanoparticles yield extremely weak CL signals, which might explain why no spatially resolved CL experiments have been previously reported on objects of such a small size.

Experiments are performed using a scanning transmission electron microscope (STEM) fitted with homemade EELS detection<sup>4</sup> and high efficiency CL detection<sup>36</sup> systems, as presented in Figure 1a. Such a microscope generates a subnanometer electron beam that can be scanned over the

region of interest. At each sampling point, a morphological (high angle annular dark field, HAADF) signal is recorded simultaneously with an EELS or a CL spectrum. At the end of the scan, both an HAADF image and a complete set of spatially resolved spectra are collected and can be accurately compared. Alternatively, such a set of spatially resolved spectra can be viewed as a collection of energy filtered maps, which show the spatial distribution of the recorded signal at constant energy (see below for examples). In these experiments, EELS and CL data sets are acquired sequentially because the experimental illumination conditions are drastically different for both spectroscopies, with electron beam currents typically 2 orders of magnitude higher for CL experiments (around 1 nA) than for EELS experiments (around 10–20 pA). Furthermore, typical acquisition times for EELS are 5 to 10 times shorter than for CL. This emphasizes the much higher interaction cross sections when measured by EELS as compared to CL.

As the purpose of the paper is to directly compare both techniques, extreme care is taken in calibrating both spectrometers. Further details can be found in the Methods section. We systematically check that the electron beam does not alter the prisms or the substrate during the scans, and we

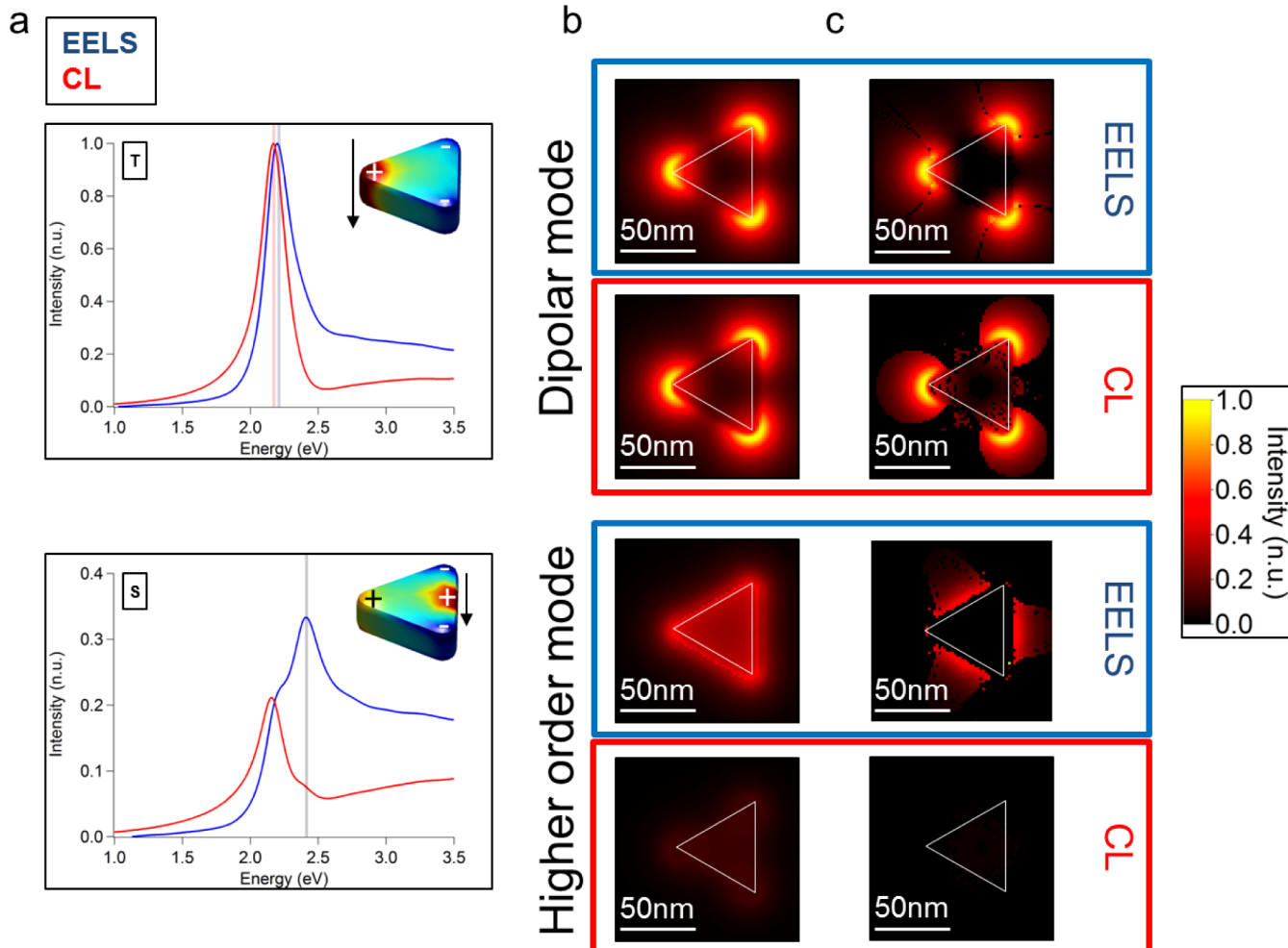


**Figure 3.** (a) Simulated EELS (blue) and CL (red) spectra calculated at the tip (T) and side (S) of a 60 nm long, 30 nm thick prism surrounded by vacuum. The windows indicate the spectral ranges considered when building the energy filtered and fitted maps of (b) and (c). Inset: surface charges induced by a fast electron beam located at the tip and side (represented as arrows) at the energies of the corresponding EELS maxima. (b) Simulated EELS and CL maps filtered around the energy of the EELS and CL maxima. (c) Simulated fitted amplitude maps corresponding to the dipolar (EELS and CL) and higher order (EELS only) modes. EELS and CL are independently normalized to their own maxima. The white lines superimposed on the maps indicate the prism shape.

discard all experiments in which this happens. We stress that we perform measurements on the very same triangles and environment, thus allowing us to unambiguously compare both physical signals (EELS and CL). This is in stark contrast to previously published CL and EELS measurements performed on related but dissimilar nanoparticles,<sup>37</sup> as even slight changes in dimensions or environment can significantly shift energies<sup>38</sup> and, thus, impair any quantitative comparison between CL and EELS.

We simulate spatially resolved EELS and CL probabilities, as well as extinction and scattering cross sections, using the retarded boundary-element method (BEM),<sup>39</sup> which allows us to account for the particle morphologies<sup>37</sup> and, when appropriate, model carbon substrates. The dielectric function of gold and amorphous carbon are taken from optical data.<sup>40,41</sup> When needed, in order to increase the effect of dissipation, the imaginary part of the dielectric functions are modified as described in ref 23 (see Methods).

As a first illustration, Figure 1b presents the HAADF image and colored maps obtained from spatially resolved EELS and CL experiments performed on a 60 nm-wide triangle lying on a graphene sheet. Total acquisition times for the whole

experiments are 157 s for CL and 16 s for EELS. In the color maps, the color and intensity of each pixel can be related to the energy and amplitude of a locally measured resonance.<sup>42</sup> These maps clearly show that two main excitations, located at the tips (lower energy excitation, yellowish color) and at the sides (higher energy excitation, greenish color) of the nanoprism, are measured in EELS, whereas only the low energy one is observed in CL. It is worth noting that such maps can be generated on the fly right after acquisition without resorting to the more lengthy procedures required for a quantitative analysis described below.

In order to quantitatively analyze the features already suggested by Figure 1b, we show in Figure 2a the EELS (blue) and CL (red) spectra corresponding to an electron probe located at the tip (T) and side (S) of this nanoprism. The filtered maps of Figure 2b display the spatial variations of the EELS (blue framed maps) and CL (red framed maps) signals averaged over two narrow (50 meV wide) energy windows centered on the resonances revealed in the EELS spectra. Beyond such filtered maps, we analyze the SP modes probed by both techniques by processing and fitting each spectrum of the data sets to a sum of Gaussian functions.<sup>43,44</sup>

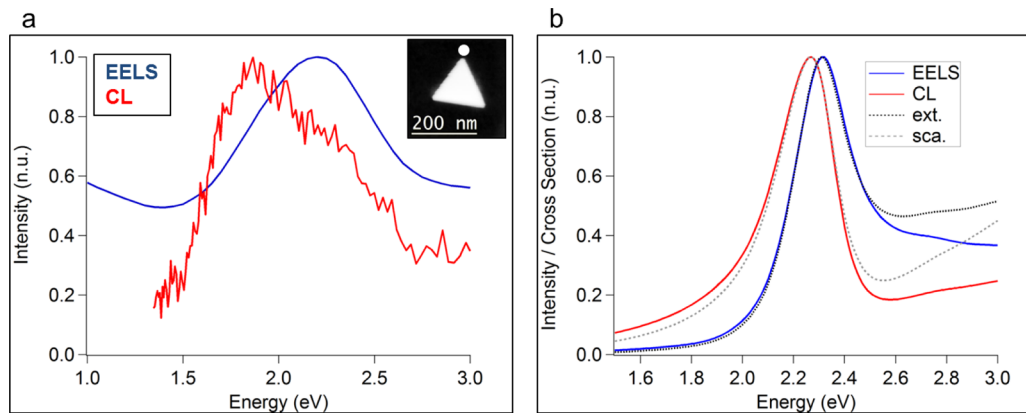


**Figure 4.** (a) Measured EELS (blue) and CL (red) spectra taken at the tip of a 140 nm edge long gold prism lying on a carbon foil. Inset: HAADF image of the nanoprism. The white disk indicates the electron beam position. (b) Calculated extinction (black dotted line) and scattering spectra (gray dotted line) superimposed to calculated EELS (blue) and CL (red) tip spectra for a single small nanoprism of 50 nm edge length, 50 nm thickness surrounded by vacuum. In the case of the optical cross sections, the light propagation direction is chosen perpendicular to the prism, and the polarization is parallel to one of the edges.

By doing so, each Gaussian peak can be associated with an optical mode.<sup>4,12,23,37,38,43,44</sup> An intensity map of a given mode is then retrieved by assigning to each image pixel the peak amplitude measured in the spectrum that is recorded at the corresponding electron probe position. Such amplitude maps are shown in Figure 2c and correspond to modes resonating at the energies associated with the maxima visible in the EELS and CL spectra. Data analysis based on such fitting techniques allows us to lift the ambiguities generally found in filtered maps, in which the origin of a given intensity change cannot be clearly identified, as it can result from a peak energy change or the tail of a neighboring intense mode (see refs 23 and 24). As already demonstrated,<sup>27,35</sup> the two dominant modes that appear in the EELS data correspond to a low-energy dipolar mode, with charge density peaking at the tips, and a higher-energy non dipolar mode, with charge density peaking at the tips and edges (see inset of Figure 3a). The nondipolar mode, loosely denoted here as a higher order mode, has been historically referred to as quadrupolar<sup>35</sup> but has been recently recast as hexapolar.<sup>20</sup> When averaging over the three tips and sides, we note that these modes are resonant at  $E_{\text{EELS}}^{\text{d,exp}} = 2.16 \pm 0.02$  eV and  $E_{\text{EELS}}^{\text{ho,exp}} = 2.41 \pm 0.02$  eV, respectively. Strikingly, the CL data exhibit just the dipolar mode (resonant at  $E_{\text{CL}}^{\text{d,exp}} = 2.18 \pm 0.02$  eV), as implied by the featureless spectrum and map filtered at the higher order mode energy, which shows only a background intensity without any spatial variations. We also note that the spatial distributions of EELS and CL intensities are similar for the dipolar mode, as suggested by previously reported EELS<sup>4,27,33</sup> and CL<sup>34</sup> separate experiments. These conclusions confirm the above qualitative analysis based in Figure 1b. The darkening of the higher order mode in CL is corroborated by the simulations shown in Figure 3. Considering the absolute energy values, the agreement between simulations and experiments is quite satisfactory without taking into account any substrate. More precisely, they show that the dipolar mode is resonant at  $E_{\text{EELS}}^{\text{d,sim}} = 2.20 \pm 0.005$  eV in EELS and  $E_{\text{CL}}^{\text{d,sim}} = 2.17 \pm 0.005$  eV in CL. Furthermore, the higher order mode appears as an additional clear peak at  $E_{\text{EELS}}^{\text{ho,sim}} = 2.41 \pm 0.005$  eV in EELS, whereas it is barely visible in CL. The small energy difference between the EELS and CL dipolar resonances, which lies within the experimental error bars, is discussed in more details further on. Moreover, we note that the full width at half-maximum (fwhm) of the calculated EELS and CL resonances ( $\sigma_{\text{EELS}}^{\text{d,sim}}$  =

$230 \pm 5$  meV) are in good agreement with those obtained from the CL measurements ( $\sigma_{\text{CL}}^{\text{d,exp}} = 245 \pm 20$  meV) but are slightly smaller than those of the EELS measurements ( $\sigma_{\text{EELS}}^{\text{d,exp}} = 260 \pm 20$  meV). We attribute this effect to the lower experimental energy resolution of EELS as compared with CL. The remarkable agreement between the experimental and calculated CL fwhm, thus, confirms the weak influence of the graphene sheet on the actual measurements. The absence of any higher order mode within the CL data set is a direct experimental demonstration of the drastically different characters of EELS and CL signals, which has been theoretically anticipated for several years.<sup>18,24,25</sup> CL only probes the radiative modes, which are dipolar modes for small objects, while EELS probes all the modes. We note that higher order modes may be radiative for larger triangles leaving the quasistatic regime.

We now focus on a more systematic comparison of EELS and CL measurements of dipolar modes in small nanoprism, before drawing a parallel with optical extinction and scattering. In the case shown in Figures 2 and 3 (small, graphene-supported particles), the dipolar energy positions as measured in EELS and CL are very similar. However, the situation is different when considering larger nanoprisms on carbon films. Although the spatial distributions of EELS and CL intensities are rather similar in both spectroscopies, just as for the smaller triangles, a difference arises for the resonance energies (see e.g., Figure S1 in Supporting Information). Figure 4a shows experimental EELS and CL spectra recorded when the electron probe is located at the tip of a nanoprism lying on a carbon foil. Although associated with the same dipolar mode, the EELS resonance is strikingly blue-shifted with respect to the CL resonance. Also, the fwhm are larger in this case than for the small triangles lying on graphene. Similar shifts and increased broadening are measured repeatedly on nanoprisms lying on a carbon foil, and are reminiscent of extinction and scattering phenomena. Indeed, as a very simple example, Figure 4b shows calculated extinction and scattering spectra superimposed on calculated EELS and CL tip spectra for an individual small nanoprism. The resemblance between EELS (CL) and extinction (scattering) is remarkable around the resonances. In particular, extinction is also blue-shifted with respect to scattering, and the shift is the same as between EELS and CL.

In order to seek a deeper and more intuitive understanding of these observations, we adopt an analytical approach derived

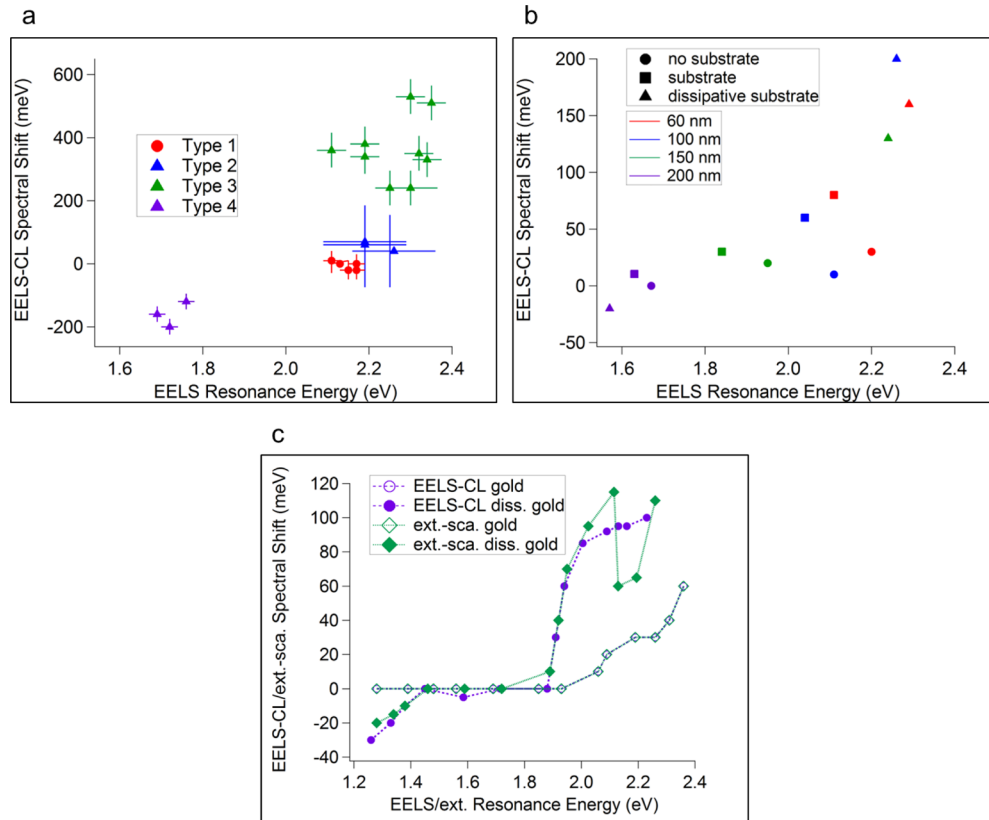


**Figure 5.** (a) EELS-CL spectral shifts as measured at the tips of several gold nanoprisms. The nanoprisms are color-sorted in four different types. Type 1: small 60 nm edge long nanoprism lying on a graphene sheet. Type 2: 90 nm edge long nanoprism lying on a carbon foil. Type 3: 130–150 nm edge long nanoprisms lying on a carbon foil. Type 4: 160 nm edge long nanoprism lying on a carbon foil. (b) EELS-CL spectral shifts as obtained from tip spectra of gold nanoprisms of various sizes simulated within the retarded BEM framework, with and without sparsely or highly dissipative carbon substrates. The nanoprisms have a constant aspect ratio of 2, and the numbers in the caption correspond to the edge lengths. (c) Spectral shifts between EELS and CL (round purple symbols), and extinction and scattering (diamond green symbols), predicted within the quasistatic modal decomposition model described in the text when using the dielectric function of ref 40. The resonances are calculated for various dipolar modes of gold objects with tabulated dissipation (unfilled symbols) and increased dissipation simulated by multiplying the imaginary part of the tabulated dielectric function by a factor of 5 (filled symbols). The resonance energies are tuned by changing the eigenvalue  $\lambda_i$  (see text). Note that in the case of low dissipation, there is no visible difference between EELS (CL) and extinction (scattering).

from the nonretarded BEM formalism in the quasistatic limit<sup>12,14,15,18,19</sup> (see Supporting Information for a more detailed description and the complete derivation). This formalism enables a direct comparison between the quantities measured by optical and fast electron based spectroscopies through simple analytical expressions. In particular, the absorption and scattering cross sections can be shown to reduce to  $C_{\text{abs}}(\omega) = \sum_{i=d} A_{i,\text{abs}} \omega \text{Im}\{f_i(\omega)\}$  and  $C_{\text{sca}}(\omega) = \sum_{i=d} A_{i,\text{sca}} \omega^4 |f_i(\omega)|^2$ , where  $A_{i,\text{abs}}$  and  $A_{i,\text{sca}}$  are energy-independent prefactors and

$$f_i(\omega) = \frac{\lambda_i + 1}{\lambda_i - \lambda(\omega)} \quad (1)$$

In this expression,  $\lambda_i$  is a real eigenvalue characterizing mode  $i$ , and  $\lambda(\omega) = (1 + \varepsilon(\omega))/(1 - \varepsilon(\omega))$  contains the dielectric function of the metallic object  $\varepsilon(\omega)$ . The physical meanings of the spectral function  $f_i(\omega)$  and of  $\lambda_i$  can be found in refs 12, 15, and 24. In the modal decompositions, the sums run over all the dipolar modes of the system. Obviously, the extinction and absorption cross sections are the same,<sup>45</sup> as the scattering cross section vanishes in the quasistatic limit. Thus, the physics of extinction is driven by absorption, and we can place extinction and absorption on an equal footing. Furthermore, it has been

shown that the EEL probability at point  $\vec{R}_\perp$  in a plane perpendicular to the electron beam (along  $z$ ) reduces to<sup>12</sup>

$$\Gamma_{\text{EEL}}(\vec{R}_\perp, \omega) = A_{\text{EEL}} \sum_i \text{Im}\{f_i(\omega)\} \left| \tilde{\phi}_i(\vec{R}_\perp, \frac{\omega}{v}) \right|^2 \quad (2)$$

where  $A_{\text{EEL}}$  is an energy-independent prefactor and  $\tilde{\phi}_i(\vec{R}_\perp, q_z)$  is the Fourier transform of the eigenpotential of mode  $i$   $\phi_i(\vec{R}_\perp, z)$  along the beam direction. In a similar way, one can write the CL probability as

$$\Gamma_{\text{CL}}(\vec{R}_\perp, \omega) \approx \sum_{i=d} A_{i,\text{CL}} \omega^3 |f_i(\omega)|^2 \left| \tilde{\phi}_i(\vec{R}_\perp, \frac{\omega}{v}) \right|^2 \quad (3)$$

where  $A_{i,\text{CL}}$  is an energy-independent prefactor. In contrast to EELS, the sum only runs over the dipolar modes (i.e., the only ones that contribute to radiation in the small particle limit).

Equations 2 and 3 show that for a given dipolar mode  $i$ , the spatial dependences are the same in EELS and CL, as observed experimentally and in the simulations. They have a well-defined physical meaning, given by the spatial modulations of  $|\tilde{\phi}_i(\vec{R}_\perp, \omega/v)|^2$ . Furthermore, the above expressions clearly reveal that the spectral profiles of both EELS and absorption/extinction are proportional to the same spectral function  $\text{Im}\{f_i(\omega)\}$ . Likewise,

CL and scattering are both proportional to  $|f_i(\omega)|^2$ . This finding constitutes a generalization to an arbitrary shape of a well-known result in the special case of a small sphere<sup>16,24,45</sup> and explains in simple terms why EELS and extinction on the one hand and CL and scattering on the other are so closely related. Indeed, although both the square modulus and imaginary parts of  $f_i(\omega)$  have the exact same maximum energies in the absence of dissipation, they shift when dissipation is present. For instance, by inserting a Drude model expression  $\epsilon(\omega) = 1 - \omega_p^2/(\omega^2 + i\Gamma\omega)$  ( $\omega_p$  being the bulk plasmon energy and  $\Gamma$  a damping term) into eq 1, one finds the following Lorentzian-type expressions for the imaginary part and square modulus of  $f_i(\omega)$

$$\text{Im}\{f_i(\omega)\} = \frac{\Gamma\tilde{\omega}_i^2\omega}{\Gamma^2\omega^2 + (\omega^2 - \tilde{\omega}_i^2)^2} \quad (4)$$

$$|f_i(\omega)|^2 = \frac{\tilde{\omega}_i^4}{\Gamma^2\omega^2 + (\omega^2 - \tilde{\omega}_i^2)^2} \quad (5)$$

where  $\tilde{\omega}_i = \sqrt{1 + \lambda_i}\omega_p/\sqrt{2}$  is the well-known nondissipative SP energy, which has a simple dependence on  $\lambda_i$  in the Drude model. Because with this analytical dielectric constant  $\text{Im}\{f_i(\omega)\} \propto \omega|f_i(\omega)|^2$ , it is clear that these two quantities do not have the same resonance energies. This is consistent with the observation that the maximum oscillation amplitude of a driven harmonic damped oscillator (which corresponds to the maximum dipole moment and, thus, can be connected to the light emission induced either by light or fast electrons) occurs at a lower frequency than the maximum energy transfer.<sup>46</sup> Such effect has been invoked to explain the spectral shifts between near-field probe and far-field spectra<sup>47</sup> and has already been reported theoretically for extinction and scattering.<sup>48</sup> These expressions also predict that the magnitude of the shift increases with the amount of dissipation, which is in agreement with the fact that a shift is measured between EELS and CL only on large particles lying on a carbon foil.

As a further investigation of such spectral shifts, Figure 5a shows the magnitude of the EELS-CL shifts as measured on different particles. We sort these particles into four different groups: very small particles (60 nm edge long) lying on a graphene sheet (type 1), and larger particles of various sizes (90 nm, 130–150 nm, and 160 nm edge long) lying on a carbon foil (types 2, 3, and 4, respectively). We can speculate two different reasons to explain the shifts: large particle sizes and absorbing substrate. Thus, we perform additional retarded BEM simulations for gold nanoprisms with different sizes, with and without sparsely or highly dissipative carbon substrates (see Methods). For simplicity, we keep a constant aspect ratio of 2 and vary the edge length. The output is summarized in Figure 5b. For a given size, the substrate either induces or increases the spectral shift between EELS and CL by an amount related to its dissipating influence, in accordance with the quasistatic theory. We stress that the exact energy positions and shifts depend both on the size of the object and the absorption properties of the substrate, which makes any truly quantitative comparison between experiments and simulations extremely difficult. In particular, the thickness of most of the objects, as well as the exact dielectric properties of the substrate and environment, are unknown. As a matter of fact, the magnitude of the shift is always much larger in experiments than in simulations, which we tentatively attribute to an underestimate of dissipation. However, it is striking that the calculated trend is in qualitative

agreement with the experiment (compare Figure 5a and b). Interestingly, this trend cannot be captured by our model when describing the metal with a simple Drude model. In particular, taking into account the right energy dependent prefactors of the modal decompositions, eqs 4 and 5 imply that a dipolar mode would induce a CL (scattering) resonance blue-shifted relative to its corresponding EELS (extinction) resonance, which is contrary to what is observed in most of the cases. Nevertheless, the complete trend is qualitatively recovered by the model, not only for EELS and CL but also for extinction and scattering, when introducing tabulated gold dielectric function<sup>40</sup> into eq 1 (see Figure 5c). This points out the importance of taking into account interband transitions in gold in this energy range to accurately describe the difference between absorption and scattering phenomena. This trend can be summarized as follows: the shift between EELS/extinction and CL/scattering, whose magnitude increases with the dissipation level, is increasingly negative below typically 1.6 eV, where gold behaves as a good Drude metal, and is increasingly positive above 1.8 eV, where it is dominated by its interband transitions.<sup>49</sup> The quasistatic modal decompositions are thus capable of generally explaining the close similarities between EELS and extinction shown in recent experiments<sup>50</sup> and call for an experimental comparison of CL and scattering to confirm their predicted resemblance.

In conclusion, we report spatially resolved EELS and CL measurements on the very same gold nanoprisms. They lead to the possibility of directly sorting out radiative and nonradiative modes. We show that a radiative mode, depending on the size and substrate, may be clearly observable at different resonance energies in both EELS and CL. These results are in agreement with fully retarded BEM electromagnetic simulations, which also indicate that such spectral differences originate in dissipation and are similar to those observed between optical extinction and scattering. These observations are explained using a modal decomposition analysis, which allows us to link the macroscopic concepts of extinction and scattering to spatially resolved EELS and CL experiments. We expect that these conclusions can be extrapolated to larger particles, for which similar retarded modal decompositions are needed to deal with more delocalized SP modes. We further hope that the present work sheds some light on the experimental retrieval of spectral and spatial information on plasmons.

**Methods.** The experiments are performed using a Vacuum Generator HB-501 scanning transmission electron microscope (STEM) equipped with a cold field emission electron gun. Both CL and EELS measurements are carried out at an operation voltage of 100 kV. The incident electron beam semiangle for EELS is set to 7.5 mrad, resulting in typical currents of 10–20 pA for a probe size of 0.7 nm. The incident semiangle for CL is set to 15 mrad, resulting in currents of more than 1 nA and a probe size of a few nanometres. The collection semiangle is 9 mrad for EELS, whereas the solid detection angle is  $1.2\pi$  sterad for CL.

Small monodisperse and larger nanoprisms are measured. The larger nanoprisms are dropcasted on a standard TEM grid, whereas the small ones are dropcasted on graphene sheets (Ted Pella Single Layer Graphene). The thickness of the monodisperse nanoprisms is monitored by deliberately damaging the graphene sheet by extreme illumination conditions. This leads to the deterioration of the sheet and the subsequent tilt of the nanoprism.

The dispersion of the electron and optical spectrometers are carefully measured through different calibration procedures. The EELS calibration is performed by applying a 10 V voltage difference on the drift tube and measuring the resulting spectral shift of the zero loss peak (ZLP) of an averaged spectrum recorded in vacuum (vacuum ZLP). The CL calibration is performed by systematically recording an Hg lamp emission spectrum after the experiments.

After acquisition, the EELS spectra are spectrally aligned and binned together. The resulting set of spectra is then deconvolved by the vacuum ZLP through Richardson Lucy deconvolution.<sup>51</sup> The dark noise of the CCD camera together with a very small signal contribution coming from the substrate are removed from the CL spectra by averaging and subtracting a few spectra recorded from the substrate.

After deconvolution, the spectral resolution for EELS, as estimated from the fwhm of the deconvolved vacuum ZLP, is of the order of 150 meV. The spectral resolution for CL is of the order of 30 meV, as estimated from the fwhm of the emission lines of the Hg lamp.

The EELS and CL local spectra shown on this article are averaged over a few pixels around the locations shown on the images. They are fitted to a single Gaussian function plus a sigmoid background to precisely access the resonance energies. All along this article, the errors given for each resonance include the calibration error as well as a possible fitting error. When the resonance energies and peak fwhm associated with the dipolar and higher order modes are discussed, the values also take into account an average over the resonances as measured at the three tips and sides of the nanoprisms. In order to build maps such as the ones used in Figures 1 and 2, all the EELS spectra contained in the spatially resolved data set are first normalized and subtracted from the ZLP.<sup>4</sup> Prior to fitting, the noise of the CL spectra is reduced via principal component analysis.<sup>52</sup> Multipole fitting is performed on both EELS and CL data sets using a sum of Gaussian functions and a sigmoid background within each spectrum.<sup>38</sup> Maps of the amplitude of those peaks whose central energy is found within a given energy range are produced by assigning to each probe position the amplitude of the Gaussian function that is fitted within the corresponding spectrum in this energy range. For all the maps shown in this paper, we make sure that only one fitted Gaussian function has its center in the selected, narrow energy range.

The boundary element method (BEM) numerical simulations are achieved using either BEM-3D<sup>37</sup> or the MNPBEM toolbox<sup>53</sup> with its EELS/CL extension,<sup>54</sup> with the CL spectra computed as described in ref 55. Simulations including a substrate are performed by adding a 5 nm thin cylinder upon which the nanoprisms stands completely. To account for additional dissipation of the substrate, we arbitrarily multiply the imaginary part of the dielectric function of amorphous carbon<sup>41</sup> by 2. The amplitude maps of Figure 3c are obtained by calculating complete EELS and CL spectra at different probe positions and applying the same fitting procedure as for the experiment.

## ■ ASSOCIATED CONTENT

### Supporting Information

Further experiments, theoretical derivations and detailed interpretations are provided in Supporting Information. This material is available free of charge via the Internet at <http://pubs.acs.org/>.

## ■ AUTHOR INFORMATION

### Corresponding Author

\*E-mail: kociak@lps.u-psud.fr.

### Notes

The authors declare no competing financial interest.

## ■ ACKNOWLEDGMENTS

This work has received support from the French State managed by the National Agency for Research under the program of future investment EQUIPEX TEMPOS-CHROMATEM with the reference ANR-10-EQPX-50, the HYNNA project, as well as the French General Directorate for Armament. The research leading to these results has received funding from the European Union Seventh Framework Programme [No. FP7/2007-2013] under Grant Agreement No. n312483 (ESTEEM2). L.F.Z. acknowledges funding from the São Paulo Research Foundation (FAPESP), grants 2011/05989-5 and 2013/06167-4. V.M. acknowledges financial support through JAE from CSIC. L.M.L.-M. acknowledges funding from the European Research Council Advanced Grant PLASMAQUO (No. 267867). M.K. and A.L. want to thank S. Meuret for help in designing test samples not presented in this study and U. Hohenester for advice in setting substrate simulations using the MNPBEM toolbox. The authors also appreciate financial support from the European Union under the Seventh Framework Program (Integrated Infrastructure Initiative N. 262348 European Soft Matter Infrastructure, ESMI).

## ■ REFERENCES

- (1) Batson, P. *Phys. Rev. Lett.* **1982**, *49*, 936–940.
- (2) Weeber, J.-C.; Dereux, A.; Girard, C.; Krenn, J. R.; Goudonnet, J.-P. *Phys. Rev. B* **1999**, *60*, 9061–9068.
- (3) Yamamoto, N.; Araya, K.; García de Abajo, F. J. *Phys. Rev. B* **2001**, *64*(20), 205419.
- (4) Nelayah, J.; Kociak, M.; Stéphan, O.; García de Abajo, F. J.; Tence, M.; Henrard, L.; Taverna, D.; Pastoriza-Santos, I.; Liz-Marzán, L. M.; Colliex, C. *Nat. Phys.* **2007**, *3*, 348–353.
- (5) Bosman, M.; Keast, V. J.; Watanabe, M.; Maaroof, A. I.; Cortie, M. B. *Nanotechnology* **2007**, *18*, 165505.
- (6) Vesseur, E. J. R.; de Waele, R.; Kuttge, M.; Polman, A. *Nano Lett.* **2007**, *7*, 2843–2846.
- (7) Douillard, L.; Charra, F.; Korczak, Z.; Bachelot, R.; Kostcheev, S.; Lerondel, G.; Adam, P. M.; Royer, P. *Nano Lett.* **2008**, *8*, 935–940.
- (8) Rossouw, D.; Couillard, M.; Vickery, J.; Kumacheva, E.; Botton, G. A. *Nano Lett.* **2011**, *11*, 1499–1504.
- (9) Joulain, K.; Carminati, R.; Mulet, J. P.; Greffet, J. J. *Phys. Rev. B* **2003**, *68*, 245405.
- (10) Stockman, M.; Faleev, S.; Bergman, D. *Phys. Rev. Lett.* **2001**, *87*, 167401.
- (11) Dereux, A.; Girard, C.; Weeber, J. C. *J. Chem. Phys.* **2000**, *112*, 7775–7789.
- (12) Boudarham, G.; Kociak, M. *Phys. Rev. B* **2012**, *85*, 245447.
- (13) De Wilde, Y.; Formanek, F.; Carminati, R.; Gralak, B.; Lemoine, P. A.; Joulain, K.; Mulet, J. P.; Chen, Y.; Greffet, J. J. *Nature* **2006**, *444*, 740–743.
- (14) Ouyang, F.; Isaacson, M. *Philos. Mag. B* **1989**, *60*, 481–492.
- (15) García de Abajo, F. J.; Aizpurua, J. *Phys. Rev. B* **1997**, *56*, 15873–15884.
- (16) García de Abajo, F. J. *Phys. Rev. B* **1999**, *59*, 3095–3107.
- (17) García de Abajo, F. J.; Kociak, M. *Phys. Rev. Lett.* **2008**, *100*, 106804.
- (18) Hohenester, U.; Ditzbacher, H.; Krenn, J. R. *Phys. Rev. Lett.* **2009**, *103*, 106801.
- (19) Hörl, A.; Trügler, A.; Hohenester, U. *Phys. Rev. Lett.* **2013**, *111*, 076801.

- (20) Schmidt, F. P.; Ditlbacher, H.; Hofer, F.; Krenn, J. R.; Hohenester, U. *Nano Lett.* **2014**, *14*, 4810–4815.
- (21) Vesseur, E. J. R.; García de Abajo, F. J.; Polman, A. *Nano Lett.* **2009**, *9*, 3147–3150.
- (22) Kuttge, M.; Vesseur, E. J. R.; Koenderink, A. F.; Lezec, H. J.; Atwater, H. A.; García de Abajo, F. J.; Polman, A. *Phys. Rev. B* **2009**, *79*, 113405.
- (23) Losquin, A.; Camelio, S.; Rossouw, D.; Besbes, M.; Pailloux, F.; Babonneau, D.; Botton, G. A.; Greffet, J.-J.; Stéphan, O.; Kociak, M. *Phys. Rev. B* **2013**, *88*, 115427.
- (24) Kociak, M.; Stephan, O. *Chem. Soc. Rev.* **2014**, *43*, 3865–3883.
- (25) García de Abajo, F. J. *Rev. Mod. Phys.* **2010**, *82*, 209–275.
- (26) Gomez-Medina, R.; Yamamoto, N.; Nakano, M.; García de Abajo, F. J. *New J. Phys.* **2008**, *10*, 105009.
- (27) Nelayah, J.; Kociak, M.; Stéphan, O.; Geuquet, N.; Henrard, L.; García de Abajo, F. J.; Pastoriza-Santos, I.; Liz-Marzan, L. M.; Colliex, C. *Nano Lett.* **2010**, *10*, 902–907.
- (28) Bigelow, N. W.; Vaschillo, A.; Camden, J. P.; Masiello, D. J. *ACS Nano* **2013**, *7*, 4511–4519.
- (29) Collins, S. M.; Midgley, P. A. *Phys. Rev. B* **2013**, *87*, 235432.
- (30) Collins, S. M.; Nicoletti, O.; Rossouw, D.; Ostasevicius, T.; Midgley, P. A. *Phys. Rev. B* **2014**, *90*, 155419.
- (31) Sanchez-Iglesias, A.; Pastoriza-Santos, I.; Perez-Juste, J.; Rodriguez Gonzalez, B.; Garcia de Abajo, F. J.; Liz-Marzan, L. M. *Adv. Mater.* **2006**, *18*, 2529–2534.
- (32) Scarabelli, L.; Coronado-Puchau, M.; Giner-Casares, J. J.; Langer, J.; Liz-Marzán, L. M. *ACS Nano* **2014**, *8*, 5833–5842.
- (33) Gu, L.; Sigle, W.; Koch, C. T.; Ogut, B.; van Aken, P. A.; Talebi, N.; Vogelgesang, R.; Mu, J. L.; Wen, X. G.; Mao, J. *Phys. Rev. B* **2011**, *83*, 195433.
- (34) Das, P.; Chini, T. K.; Pond, J. *J. Phys. Chem. C* **2012**, *116*, 5610–15619.
- (35) Hao, E.; Schatz, G. C. *J. Chem. Phys.* **2004**, *120*, 357–366.
- (36) Zagonel, L. F.; Mazzucco, S.; Tencé, M.; March, K.; Bernard, R.; Laslier, B.; Jacopin, G.; Tchernycheva, M.; Rigutti, L.; Julien, F. H.; Songmuang, R.; Kociak, M. *Nano Lett.* **2011**, *11*, 568–573.
- (37) Myroshnychenko, V.; Nelayah, J.; Adamo, G.; Geuquet, N.; Rodriguez-Fernandez, J.; Pastoriza-Santos, I.; MacDonald, K. F.; Henrard, L.; Liz-Marzan, L. M.; Zheludev, N. I.; Kociak, M.; García de Abajo, F. J. *Nano Lett.* **2012**, *12*, 4172–4180.
- (38) Mazzucco, S.; Geuquet, N.; Ye, J.; Stéphan, O.; Van Roy, W.; Van Dorpe, P.; Henrard, L.; Kociak, M. *Nano Lett.* **2012**, *12*, 1288–1294.
- (39) García de Abajo, F. J.; Howie, A. *Phys. Rev. B* **2002**, *65*, 115418.
- (40) Johnson, B.; Christy, R. W. *Phys. Rev. B* **1972**, *6*, 4370–4379.
- (41) Hagemann, H.-J.; Gudat, W.; Kunz, C. *J. Opt. Soc. Am.* **1975**, *65*, 742–744.
- (42) Bosman, M.; Anstis, G. R.; Keast, V. J.; Clarke, J. D.; Cortie, M. B. *ACS Nano* **2012**, *6*, 319–326.
- (43) Mazzucco, S.; Stephan, O.; Colliex, C.; Pastoriza-Santos, I.; Liz-Marzan, L. M.; García de Abajo, F. J.; Kociak, M. *Eur. Phys. J.: Appl. Phys.* **2011**, *54*, 33512.
- (44) Bosman, M.; Ye, E.; Tan, S. F.; Nijhuis, C. A.; Yang, J. K. W.; Marty, R.; Mlayah, A.; Arbouet, A.; Girard, C.; Han, M.-Y. *Sci. Rep.* **2013**, *3*, 1312.
- (45) Bohren, C. F.; Huffman, D. R. *Absorption and scattering of light by small particles*; Wiley: New York, 1983.
- (46) Zuloaga, J.; Nordlander, P. *Nano Lett.* **2011**, *11*, 1280–1283.
- (47) Alonso-González, P.; Al bella, P.; Neubrech, F.; Huck, C.; Chen, J.; Golmar, F.; Casanova, F.; Hueso, L. E.; Pucci, A.; Aizpurua, J.; Hillenbrand, R. *Phys. Rev. Lett.* **2013**, *110*, 203902.
- (48) Kats, M. A.; Yu, N.; Genevet, P.; Gaburro, Z.; Capasso, F. *Opt. Express* **2011**, *19*, 21748–21753.
- (49) Etchegoin, P. G.; Le Ru, E. C.; Meyer, M. *J. Chem. Phys.* **2006**, *125*, 164705.
- (50) Husnik, M.; von Cube, F.; Irsen, S.; Linden, S.; Niegemann, J.; Busch, K.; Wegener, M. *Nanophotonics* **2013**, *2*, 241–245.
- (51) Gloter, A.; Douiri, A.; Tence, M.; Colliex, C. *Ultramicroscopy* **2003**, *96*, 385–400.
- (52) Edwards, P. R.; Sleith, D.; Wark, A. W.; Martin, R. W. *J. Phys. Chem. C* **2011**, *115*, 14031–14035.
- (53) Hohenester, U.; Trugler, A. *Comput. Phys. Commun.* **2012**, *183*, 370–381.
- (54) Hohenester, U. *Comput. Phys. Commun.* **2014**, *185*, 1177–1187.
- (55) Martin, J.; Kociak, M.; Mahfoud, Z.; Proust, J.; Gérard, D.; Plain, J. *Nano Lett.* **2014**, *14*, 5517–5523.

# **Supporting Information for**

## **Unveiling nanometer scale extinction and**

## **scattering phenomena through combined**

## **electron energy loss spectroscopy and**

## **cathodoluminescence measurements**

Arthur Losquin,<sup>†,‡</sup> Luiz F. Zagonel,<sup>†,¶</sup> Viktor Myroshnychenko,<sup>§,||</sup> Benito Rodríguez-Gonzalez,<sup>⊥</sup> Marcel Tencé,<sup>†</sup> Leonardo Scarabelli,<sup>⊥</sup> Jens Förstner,<sup>||</sup> Luis M. Liz-Marzán,<sup>⊥,#,△</sup> F. Javier García de Abajo,<sup>@,∇</sup> Odile Stéphan,<sup>†</sup> and Mathieu Kociak<sup>\*,†</sup>

*Laboratoire de Physique des Solides CNRS/UMR8502, Bâtiment 510, Univ. Paris-Sud, Orsay, 91405, France, Department of Physics, Lund University, P.O. Box 118, SE-221 00 Lund, Sweden, Instituto de Física Gleb Wataghin, Universidade Estadual de Campinas, Unicamp, Campinas, SP, 13083-970, Brazil, IQFR-CSIC, Serrano 119, 28006 Madrid, Spain, Institute of Electrical Engineering, University of Paderborn, Warburger Strasse 100, D-33098 Paderborn, Germany, Departamento de Química Física, Universidad de Vigo, 36310 Vigo, Spain, Bionanoplasmonics Laboratory, CIC biomaGUNE, Paseo de Miramón 182, 20009 Donostia - San Sebastián, Spain, and ICFO-Institut de Ciencies Fotoniques, Mediterranean Technology Park, 08860 Castelldefels (Barcelona), Spain*

E-mail: kociak@lps.u-psud.fr

## Additional measurements

In the article, we claim that the dipolar modes of gold nanoprisms lying on a carbon foil give rise to the same spatial distributions in EELS and CL while being resonant at different energies. An example is shown here for illustration. Figure S1a shows the HAADF image of a gold nanoprim lying on carbon, as well as EELS and CL spectra acquired for an electron probe position located at the tip. In this case, the CL resonance energy is slightly blueshifted as compared to the EELS resonance energy. Figure S1b shows the maps filtered at the energies corresponding to the EELS and CL maxima, as well as the fitted amplitude maps of the EELS and CL peaks which are respectively resonant at the resonant energies appearing in the EELS and CL spectra. These maps show unambiguously that both the EELS and CL resonances, although slightly different, are associated to the same dipolar mode.

## Theoretical derivation of the quasistatic modal decompositions

In the following, we adopt an analytical approach derived from the non-retarded BEM formalism in the quasistatic limit,<sup>1–5</sup> essentially consisting in using a rigorous eigenmode expansion

---

\*To whom correspondence should be addressed

<sup>†</sup>Laboratoire de Physique des Solides CNRS/UMR8502, Bâtiment 510, Univ. Paris-Sud, Orsay, 91405, France

<sup>‡</sup>Department of Physics, Lund University, P.O. Box 118, SE-221 00 Lund, Sweden

<sup>¶</sup>Instituto de Física Gleb Wataghin, Universidade Estadual de Campinas, Unicamp, Campinas, SP, 13083-970, Brazil

<sup>§</sup>IQFR-CSIC, Serrano 119, 28006 Madrid, Spain

<sup>||</sup>Institute of Electrical Engineering, University of Paderborn, Warburger Strasse 100, D-33098 Paderborn, Germany

<sup>⊥</sup>Departamento de Química Física, Universidade de Vigo, 36310 Vigo, Spain

<sup>#</sup>Bionanoplasmonics Laboratory, CIC biomaGUNE, Paseo de Miramón 182, 20009 Donostia - San Sebastián, Spain

<sup>®</sup>ICFO-Institut de Ciencies Fotoniques, Mediterranean Technology Park, 08860 Castelldefels (Barcelona), Spain

<sup>△</sup>Ikerbasque, Basque Foundation for Science, Bilbao, Spain

<sup>▽</sup>ICREA-Institució Catalana de Recerca i Estudis Avançats, Passeig Lluís Companys, 23, 08010 Barcelona, Spain

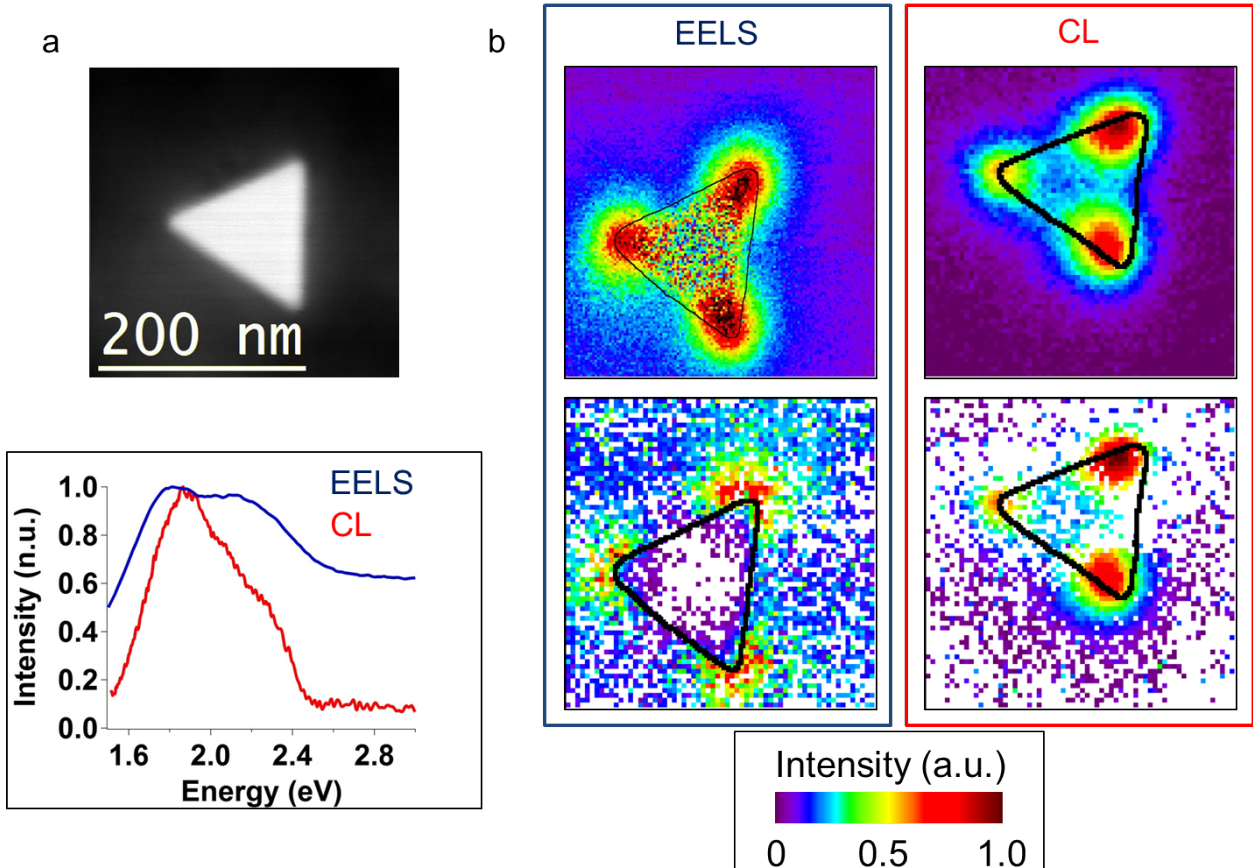


Figure 1: a. HAADF image of a gold triangular nanoprism. Experimental EELS and CL spectra corresponding to electron probe positions located at the upper tip. b. EELS and CL maps filtered at the energies of the main EELS and CL maxima (top). Fitted amplitude maps corresponding to the peaks resonant at the energies of the main EELS and CL maxima (bottom).

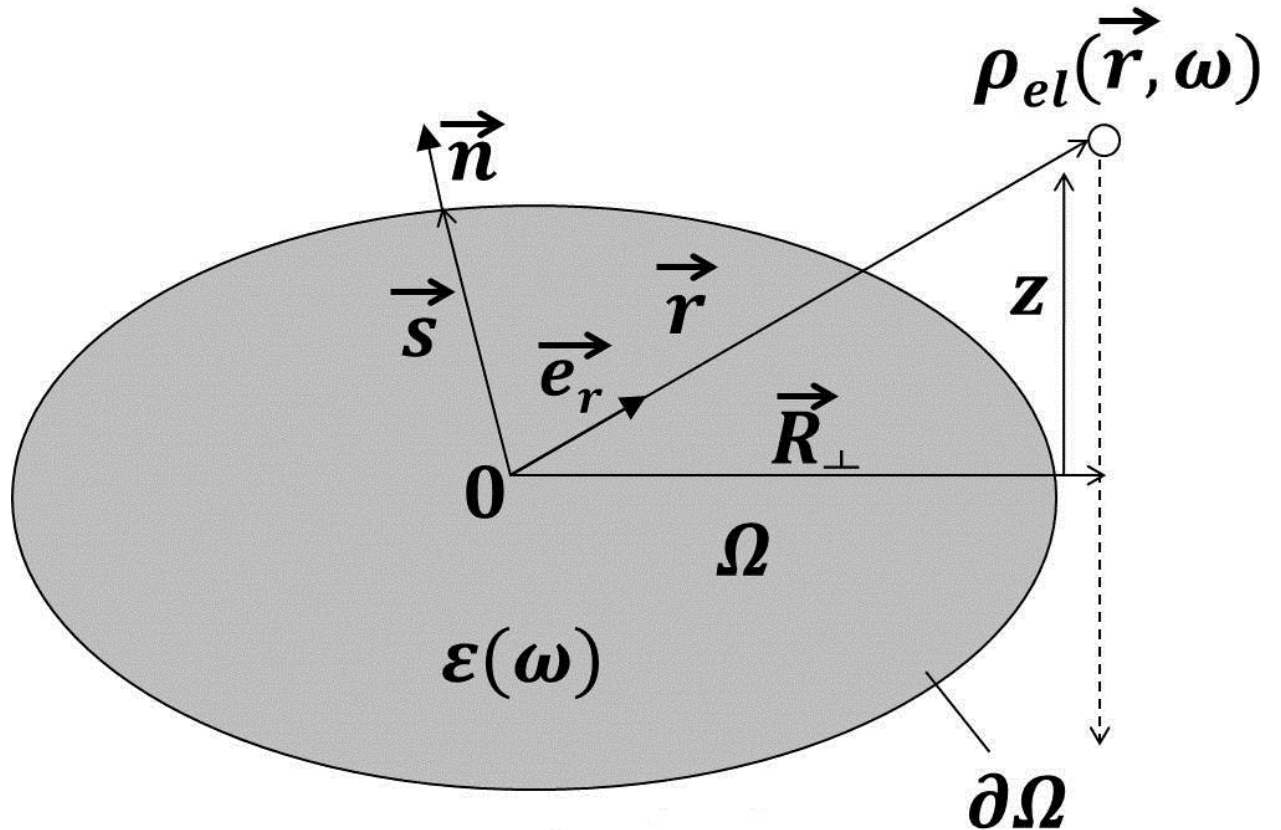


Figure 2: Schematic representation of a generic 3D system consisting of an object  $\Omega$  of dielectric function  $\epsilon(\omega)$  surrounded by vacuum. Here,  $O$  denotes the origin of the space coordinates,  $\vec{r}$  is an arbitrary coordinate vector,  $\vec{s}$  is a vector pointing to the surface  $\partial\Omega$ , and  $\vec{n}$  is a normal unit vector located at the surface position  $\vec{s}$  and pointing outside the object. An electron travelling at a distance  $\vec{R}^\perp$  from the origin along the  $z$  direction is modelled through an electric charge density  $\rho_{el}(\vec{r}, \omega)$ .

of the surface charge induced by a given excitation that is valid for any homogeneous, arbitrarily shaped object. For the sake of simplicity, we restrict the model to objects in vacuum. However, the effect of dissipation, which we want to address, is partly taken into account through the imaginary part of the dielectric function of the object itself. We consider an object of permittivity  $\epsilon(\omega)$  surrounded by vacuum, and make use of the notation introduced in Figure S2. In the quasistatic limit, the interaction between an external charge and the object can be studied by solving the Poisson equation

$$\vec{\nabla} \cdot [\tilde{\epsilon}(\vec{r}, \omega) \vec{\nabla} \phi(\vec{r}, \omega)] = -4\pi \rho_{ext}(\vec{r}, \omega), \quad (1)$$

where  $\phi(\vec{r}, \omega)$  is the electric potential expressed in time-Fourier space,

$$\tilde{\epsilon}(\vec{r}, \omega) = \begin{cases} \epsilon(\omega) & \vec{r} \in \Omega \\ 1 & \vec{r} \notin \Omega \\ \frac{1}{2} [1 + \epsilon(\omega)] & \vec{r} \in \partial\Omega \end{cases} \quad (2)$$

is a space and frequency dependent dielectric function, and  $\rho_{ext}(\vec{r}, \omega)$  is the external charge (see Figure S2). In what follows, we adopt a boundary equation method (BEM) which consists in expressing the electric potential in terms of surface-charge distributions located at the boundaries of the object.<sup>4</sup> This allows us to interpret the interaction between a given excitation and the object through the excitation of surface eigenmodes.<sup>2</sup>

## Optical properties

The optical properties can be calculated by considering setting the external charge to zero while introducing an external potential source.<sup>6,7</sup> The solution of the Poisson equation is then:

$$\phi(\vec{r}, \omega) = \phi^{ext}(\vec{r}, \omega) + \phi^{sca}(\vec{r}, \omega), \quad (3)$$

where  $\vec{E}^{ext}(\omega) = -\vec{\nabla}\phi^{ext}(\vec{r}, \omega)$  is the external field and  $\phi^{sca}(\vec{r}, \omega)$  is the scattered electric potential. We express the latter as a function of the induced surface charge distribution  $\sigma(\vec{s}, \omega)$  as

$$\phi^{sca}(\vec{r}, \omega) = \oint_{\partial\Omega} d\vec{s} \frac{\sigma(\vec{s}, \omega)}{|\vec{r} - \vec{s}|}. \quad (4)$$

Expanding  $\sigma(\vec{s}, \omega)$  within the orthonormal basis of surface eigenmodes  $\sigma_i(\vec{s})$  of eigenvalues  $\lambda_i$ ,<sup>2</sup> we can write the scattered electric potential as

$$\phi^{sca}(\vec{r}, \omega) = -\frac{1}{2\pi} \sum_i \frac{1}{\lambda_i + 1} f_i(\omega) \left\langle \vec{n} \cdot \vec{E}^{ext}(\omega), \phi^i(\vec{r}) \right\rangle \phi^i(\vec{r}), \quad (5)$$

where  $\vec{n}$  denotes the unit vector located at position  $\vec{s}$  on the boundary of the object, normal to the boundary, and pointing outwards. In the above equation, we define

$$f_i(\omega) = \frac{\lambda_i + 1}{\lambda_i - \lambda(\omega)} \quad (6)$$

where

$$\lambda(\omega) = \frac{1 + \epsilon(\omega)}{1 - \epsilon(\omega)} \quad (7)$$

and

$$\left\langle \vec{n} \cdot \vec{E}^{ext}(\omega), \phi^i(\vec{r}) \right\rangle = \oint_{\partial\Omega} d\vec{s} \vec{n} \cdot \vec{E}^{ext}(\omega) \phi^i(\vec{s})^* \quad (8)$$

where

$$\phi_i(\vec{r}) = \oint_{\partial\Omega} \frac{\sigma_i(\vec{s})}{|\vec{r} - \vec{s}|} d\vec{s} \quad (9)$$

is the eigenpotential of mode  $i$ . Expanding each eigenpotential in the dipolar approximation within Eq. 5, one can express the far-field scattered electric potential as

$$\phi_{FF}^{sca}(\vec{r}, \omega) = \frac{1}{|\vec{r}|^2} \vec{p}(\omega) \cdot \vec{e}_r + o\left(\frac{1}{|\vec{r}|^2}\right), \quad (10)$$

where  $\vec{e}_r$  is a unit vector along the direction of  $\vec{r}$ ,

$$\vec{p}(\omega) = -\frac{1}{2\pi} \sum_{i=d} \frac{1}{\lambda_i + 1} f_i(\omega) \left\langle \vec{n} \cdot \vec{E}^{ext}(\omega), \phi^i(\vec{r}) \right\rangle \vec{p}_i, \quad (11)$$

and

$$\vec{p}_i = \oint_{\partial\Omega} \sigma_i(\vec{s}) \vec{s} d\vec{s}. \quad (12)$$

is the dipole moment of mode  $i$ . Notice that the sum runs only over dipolar modes, for which  $\vec{p}_i \neq \vec{0}$ . As seen from the far field, the illuminated particle is thus equivalent to a dipole of moment  $\vec{p}(\omega)$ . The extinction and absorption cross-sections are thus given by<sup>8</sup>

$$C_{abs}(\omega) = -\frac{4\pi}{|\vec{E}^{ext}(\omega)|} k \text{Im} \left\{ \vec{p}(\omega) \cdot \vec{E}^{ext}(\omega) \right\} \quad (13)$$

$$C_{sca}(\omega) = \frac{8\pi}{3} k^4 |\vec{p}(\omega)|^2 \quad (14)$$

where  $k = \frac{\omega}{c}$  is the free space wave vector. Introducing here the expression for  $\vec{p}(\omega)$  given by Eq.11, the extinction and scattering cross-sections reduce to

$$C_{abs}(\omega) = \frac{2}{c} \frac{1}{|\vec{E}^{ext}(\omega)|} \omega \sum_{i=d} \frac{1}{\lambda_i + 1} \text{Im} \{ f_i(\omega) \} \left\langle \vec{n} \cdot \vec{E}^{ext}(\omega), \phi^i(\vec{r}) \right\rangle \vec{p}_i \cdot \vec{E}^{ext}(\omega) \quad (15)$$

$$C_{sca}(\omega) \approx \frac{2}{3\pi c^4} \omega^4 \sum_{i=d} \frac{1}{(\lambda_i + 1)^2} |f_i(\omega)|^2 \left| \left\langle \vec{n} \cdot \vec{E}^{ext}(\omega), \phi^i(\vec{r}) \right\rangle \vec{p}_i \right|^2, \quad (16)$$

In the expression for the scattering cross-section, we have neglected the crossed terms involving the interaction between different modes in  $|\vec{p}(\omega)|^2$  because in most situations the spectral responses  $f_i(\omega)$  are well separated.

## Fast-electron-based spectroscopies

In a classical dynamic approach, the energy lost by a fast electron interacting with a dielectric object is described by the work performed against the electron by a scattered electric field.

Considering the electron as a point-like charge moving with constant velocity  $\vec{v}$  along a straight-line trajectory  $\vec{r} = \vec{r}_e(t) = (\vec{R}^\perp, z)$ , the electron energy-loss (EEL) probability is given by<sup>9</sup>

$$\Gamma_{EELS}(\vec{R}^\perp, \omega) = \frac{e}{\pi\hbar\omega} \int dt \Re \left\{ e^{-i\omega t} \vec{v} \cdot \vec{E}_{el}^{sca}(\vec{r}_e(t), \omega) \right\}, \quad (17)$$

where  $-e$  is the charge of the electron and  $\vec{v}$  is its velocity.  $\vec{E}_{el}^{sca}(\vec{r}, \omega)$  is the electron-induced electric field expressed in time-Fourier space. Likewise, the cathodoluminescence (CL) probability is related to the electromagnetic energy radiated into the far field, and can be calculated from<sup>9</sup>

$$\Gamma_{CL}(\vec{R}^\perp, \omega) = \frac{1}{4\pi^2\hbar k} \int_{4\pi} \left| \vec{f}_{el}(\vec{e}_r, \omega) \right|^2 d\Omega_{\vec{e}_r}, \quad (18)$$

where

$$\vec{E}_{FF,el}^{sca}(\vec{r}, \omega) = \lim_{\vec{r} \rightarrow \infty} \vec{E}_{el}^{sca}(\vec{r}, \omega) = \frac{e^{ikr}}{r} \vec{f}_{el}(\vec{e}_r, \omega) \quad (19)$$

is the far-field electron induced electric field. Following the notation introduced in the previous section and adopting the quasistatic approximation, the electron-induced electric field is obtained by inserting into the Poisson equation a source term  $\rho_{el}(\vec{r}, \omega)$  given by

$$\rho_{el}(\vec{r}, \omega) = -\frac{e}{v} \delta(\vec{R} - \vec{R}^\perp) e^{i\omega z/v} \quad (20)$$

(i.e., a time-Fourier transformed electron charge distribution). The solution of the Poisson equation thus reads<sup>2</sup>

$$\phi(\vec{r}, \omega) = \phi_{el}^{ext}(\vec{r}, \omega) + \phi_{el}^{sca}(\vec{r}, \omega), \quad (21)$$

where

$$\phi_{el}^{ext}(\vec{r}, \omega) = \int d\vec{r}' \frac{\rho_{el}(\vec{r}', \omega)}{\epsilon(\vec{r}', \omega) |\vec{r} - \vec{r}'|} \quad (22)$$

is a source screened electric potential,

$$\phi_{el}^{sca}(\vec{r}, \omega) = \oint_{\partial\Omega} d\vec{s} \frac{\sigma_{el}(\vec{s}, \omega)}{|\vec{r} - \vec{s}|} \quad (23)$$

is the electron-induced electric potential, and  $\sigma_{el}(\vec{s}, \omega)$  is the electron-induced surface charge. Expressing the electron-induced electric potential as:

$$\phi_{el}^{sca}(\vec{r}, \omega) = \int d\vec{r}' G(\vec{r}, \vec{r}', \omega) \rho_{el}(\vec{r}', \omega) \quad (24)$$

where  $G(\vec{r}, \vec{r}', \omega)$  is the scalar Green function satisfying, if  $\vec{r}'$  does not belong to the object, the modal decomposition:<sup>4</sup>

$$G(\vec{r}, \vec{r}', \omega) = - \sum_i f_i(\omega) \phi_i(\vec{r}) \phi_i^*(\vec{r}') \quad (25)$$

one finds, when considering an electron trajectory that does not penetrate the object

$$\phi_{el}^{sca}(\vec{r}, \omega) = \frac{e}{v} \sum_i f_i(\omega) \tilde{\phi}_i^*(\vec{R}^\perp, \frac{\omega}{v}) \phi_i(\vec{r}), \quad (26)$$

where  $\tilde{\phi}_i^*(\vec{R}^\perp, q)$  is the Fourier transform of  $\phi_i(\vec{r})$  along  $z$ . Writing the induced electric field as  $\vec{E}_{el}^{sca}(\vec{r}, \omega) = -\vec{\nabla} \phi_{el}^{sca}(\vec{r}, \omega)$ , the EEL probability thus reads<sup>4</sup>

$$\Gamma_{EELS}(\vec{R}^\perp, \omega) = \frac{e^2}{\pi \hbar v^2} \sum_i \text{Im} \{f_i(\omega)\} \left| \tilde{\phi}_i(\vec{R}^\perp, \frac{\omega}{v}) \right|^2. \quad (27)$$

Expanding again each eigenpotential in the dipolar approximation within Eq. 26, one can express the far-field scattered electric potential as

$$\phi_{el,FF}^{sca}(\vec{r}, \omega) = \frac{1}{|\vec{r}|^2} \vec{p}(\vec{R}^\perp, \omega) \cdot \vec{e}_r + o\left(\frac{1}{|\vec{r}|^2}\right), \quad (28)$$

where

$$\vec{p}(\vec{R}^\perp, \omega) = \frac{e}{v} \sum_{i=d} f_i(\omega) \tilde{\phi}_i^*(\vec{R}^\perp, \frac{\omega}{v}) \vec{p}_i \quad (29)$$

is the electron-induced dipole moment. Although we calculate this dipole in the electrostatic limit, we can still use it to express the scattering amplitude as:<sup>10</sup>

$$\vec{f}_{el}(\vec{e}_r, \omega) = -k^2 \vec{e}_r \times \vec{p}(\vec{R}^\perp, \omega) \times \vec{e}_r \quad (30)$$

The CL probability thus results from the electron-induced dipole moment as

$$\Gamma_{CL}(\vec{R}^\perp, \omega) = \frac{1}{4\pi^2 \hbar} k^3 \int_{4\pi} \left| \vec{p}_\perp(\vec{R}^\perp, \omega) \right|^2 d\Omega_{\vec{e}_r}, \quad (31)$$

where  $\vec{p}_\perp(\vec{R}, \omega) = \vec{p}(\vec{R}, \omega) - \vec{e}_r \cdot \vec{p}(\vec{R}, \omega) \vec{e}_r$  is the transverse component of the electron-induced dipole moment. Inserting Eq. 29 into Eq. 31 and neglecting the crossed terms  $f_i(\omega) f_j(\omega)^*$  with  $i \neq j$ , the CL probability finally reduces to

$$\Gamma_{CL}(\vec{R}^\perp, \omega) \approx \frac{e^2}{4v^2 \pi^2 \hbar c^3} \omega^3 \sum_{i=d} |f_i(\omega)|^2 \left| \int_{4\pi} \vec{p}_{i\perp} d\Omega_{\vec{e}_r} \right|^2 \left| \tilde{\phi}_i(\vec{R}^\perp, \frac{\omega}{v}) \right|^2. \quad (32)$$

where  $\vec{p}_{i\perp} = \vec{p}_i - \vec{e}_r \cdot \vec{p}_i \vec{e}_r$  is the transverse component of the dipole moment of mode i.

## Interpretation: Drude model

We here draw some interpretations of the above modal decomposition when considering a general ideal case. For a given mode, the resonance energies as measured by the techniques depend on the dielectric properties of the medium through  $f_i(\omega)$ .

We examine what happens for model SP modes by considering an ideal metal object surrounded by vacuum. In order to do this, we take  $\epsilon(\omega)$  as a Drude dielectric function:

$$\epsilon(\omega) = 1 - \frac{\omega_p^2}{\omega^2 + i\Gamma\omega} \quad (33)$$

where  $\omega_p$  is the bulk plasmon frequency and  $\Gamma$  is a phenomenological damping rate. We then find:

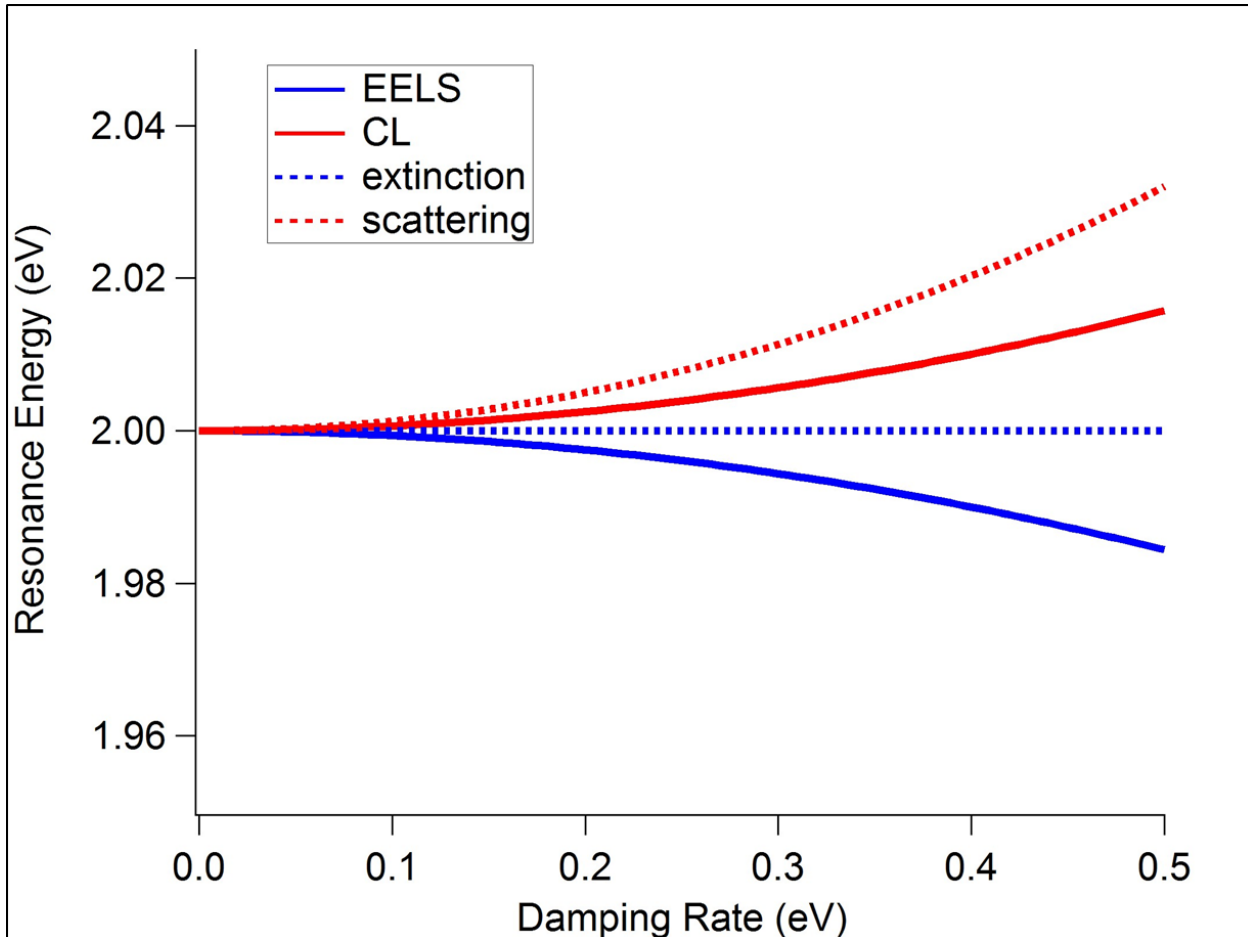


Figure 3: EELS, CL, extinction and scattering resonance energies as a function of damping rate. We take  $\tilde{\omega}_i=2.0$  eV.

$$f_i(\omega) = \frac{\tilde{\omega}_i^2}{\tilde{\omega}_i^2 - \omega^2 - i\Gamma\omega} \quad (34)$$

where:

$$\tilde{\omega}_i = \sqrt{1 + \lambda_i} \frac{\omega_p}{\sqrt{2}} \quad (35)$$

verifies  $\lambda(\tilde{\omega}_i) = \lambda_i$  in the particular case  $\Gamma = 0$ . The imaginary part and square modulus of  $f_i(\omega)$  thus read:

$$\text{Im}\{f_i(\omega)\} = \frac{\Gamma\tilde{\omega}_i^2\omega}{\Gamma^2\omega^2 + (\omega^2 - \tilde{\omega}_i^2)^2}, \quad (36)$$

$$|f_i(\omega)|^2 = \frac{\tilde{\omega}_i^4}{\Gamma^2\omega^2 + (\omega^2 - \tilde{\omega}_i^2)^2} \quad (37)$$

Making the damping rate tend towards zero, we note that:

$$\lim_{\Gamma \rightarrow 0} \text{Im}\{f_i(\omega)\} = \delta(\omega - \tilde{\omega}_i) \quad (38)$$

$$\lim_{\Gamma \rightarrow 0} |f_i(\omega)|^2 = \delta(\omega - \tilde{\omega}_i) \quad (39)$$

With no dissipation, a dipolar mode is thus resonant at its eigenenergy irrespective of the technique. However, in a general case of non-zero dissipation,  $\text{Im}\{f_i(\omega)\} \propto \omega |f_i(\omega)|^2$ , which implies that the maximum of  $\text{Im}\{f_i(\omega)\}$  is blue-shifted with respect to the maximum of  $|f_i(\omega)|^2$ . However, taking into account the right energy dependent prefactors of the modal decompositions, we note that a spectrally isolated dipole mode actually contributes to  $\Gamma_{EELS}(\vec{R}^\perp, \omega) \sim \frac{1}{\omega^2} \Gamma_{CL}(\vec{R}^\perp, \omega)$  and  $C_{ext}(\omega) \sim \frac{1}{\omega^2} C_{sca}(\omega)$ . Therefore, the CL (scattering) resonance of such mode is predicted to be blue-shifted relative to its EELS (extinction) resonance. We note that a similar conclusion has already been drawn for extinction and scattering, using a classical harmonic oscillator model, in.<sup>11</sup> Finally, this model shows that the magnitude of the shift between  $\text{Im}\{f_i(\omega)\}$  and  $|f_i(\omega)|^2$ , and, by extension, between EELS and CL and extinction and scattering, directly depends on the amount of dissipation. This

is exemplified by the resonance energies plotted as a function of the damping rate shown in Figure S3. In this particular example, we consider a single mode with  $\tilde{\omega}_i=2.0$  eV and neglect the frequency dependence of the Fourier transform of the eigenpotential in the EELS and CL expressions.

## References

- (1) Ouyang, F.; Isaacson, M. *Philos. Mag. Part B* **1989**, *60*, 481–492.
- (2) de Abajo, F. J. G.; Aizpurua, J. *Phys. Rev. B* **1997**, *56*, 15873–15884.
- (3) Hohenester, U.; Ditlbacher, H.; Krenn, J. R. *Phys. Rev. Lett.* **2009**, *103*, 106801.
- (4) Boudarham, G.; Kociak, M. *Phys. Rev. B* **2012**, *85*, 245447.
- (5) Hörl, A.; Trügler, A.; Hohenester, U. *Phys. Rev. Lett.* **2013**, *111*, 076801.
- (6) Stockman, M.; Faleev, S.; Bergman, D. *Phys. Rev. Lett.* **2001**, *87*, 167401.
- (7) Shalaev, V.; Sarychev, A. K. *Phys. Rev. B* **1998**, *57*, 13265–13288.
- (8) Bohren, C. F.; Huffman, D. R. *Absorption and scattering of light by small particles*; Wiley: New York, 1983.
- (9) de Abajo, F. J. G. *Rev. Mod. Phys.* **2010**, *82*, 209–275.
- (10) Jackson, J. D. *Classical electrodynamics*, 3rd ed.; Wiley: New York, 1999.
- (11) Kats, M. A.; Yu, N.; Genevet, P.; Gaburro, Z.; Capasso, F. *Opt. Express* **2011**, *19*, 21748–21753.